An additively manufactured fractal structure for impact absorption applications

Available online at www.sciencedirect.com

ScienceDirect

Procedia CIRP 118 (2023) 793–798

www.elsevier.com/locate/procedia

16th CIRP Conference on Intelligent Computation in Manufacturing Engineering, CIRP ICME '22, Italy

An additively manufactured fractal structure for impact absorption applications

Marco Viccica*, Manuela Galati, Flaviana Calignano, Luca Iuliano

Integrated Additive Manufacturing Center (IAM) Politecnico di Torino, Department of Management and Production Engineering (DIGEP), Torino 10129, Italy

* Corresponding author. +39-011-090-7280. E-mail address: marco.viccica@polito.it

Abstract

Today, new structural concepts have an impact on all areas of engineering, including those human safety centered. Fractals are an example of self-similar geometries designed using mathematics in an attempt to imitate nature's tested patterns. However, the complexity of the generated geometries is often too technically unfeasible to manufacture with traditional processes. The solution to this problem can be found in the additive manufacturing (AM) approach. This work proposes a novel fractal structure of high impact absorption performance for personal protective equipment applications, specifically designed for the production by AM polymeric powder bed-based technique.

Keywords: 3D Greek cross fractal; PPE; Selective laser sintering; 3d printing; PA12

1. Introduction

Chaos is generally referred to as turbulence, undesired randomness. However, over the last two decades, scientists have shown that a chaotic system can actually develop in a way that appears fluid and ordered. There is a precise moment, with a corresponding behavior, which is neither chaotic nor non-chaotic, in which the transition to chaos takes place. The analysis of this transition to chaos led to recognizing phenomena that can often be described as fractal mathematics [1]. The name fractal was coined by the mathematician Benoit Mandelbrot in 1975 [2], and it consists of a family of objects with specific features such as the same main shape on all magnification scales (self-similarity) and the pattern geometry usually irregular and chaotic [3]. Fractals in nature are everywhere. Famous examples can be recognized in coastlines, flowers, trees, and animal shells [1–6].

Since Mandelbrot [2] formalized the fractal theory, many applications have been explored in several fields such as computer graphics [7], physics [8], data security [9], surface roughness [10], mechanical transmission diagnosis [11]. Most of these studies are focused on the mathematical concept of fractal dimension. The interest in using fractal geometry to explore mechanical and thermal performance enhancements has been widely growing in the last decade. For instance, the interlocking properties of hierarchical fractal structures have been found to provide better load distribution and energy absorption [12,13]. It has been demonstrated [12] how the seam line of some structures present in biological systems is characterized by fractal-like patterns. Li et al. [12] showed that a higher hierarchy of fractal patterns resulting in a higher order of teeth produced better tensile and shear load resistance capabilities. Another example of fractal structures application is the optimization of fluid distribution through tree-like channels [14,15]. Further analysis of the tree-like fractal geometry effects was performed for crashworthiness applications [16,17]. The energy absorption capability of thin-walled tubes with bio-inspired tree-like pattern cross-sections was investigated by San Ha Ngoc et al. [17]. Many other studies were developing thin-walled tube protective devices with innovative cross-sections based on fractal structures such

10.1016/j.procir.2023.06.136

as fractal-like honeycomb [18–21], Koch curve [22], side-fractal shape [23,24], Sierpinski shape [25].

Despite all the benefits provided by using fractal geometry for specific applications, owing to their extremely high complexity, they are difficult to be manufactured or often unfeasible by traditional manufacturing technologies. The realization of a rather simple bidimensional fractal structure with a constant cross-section of geometries was completed using unconventional manufacturing methods such as wire electric discharge machine (WEDM) [17,19,22,24].

In the last decades, the development of additive manufacturing (AM) processes unlocked certain design opportunities, potentially giving more freedom to realizing such complex structures [26]. However, literature is still lacking, and only a few works investigated the adoption of AM processes but are limited to 2D geometries [13,17,23,25].

This work applies an polymer-based AM process for developing a three-dimensional (3D) Greek cross fractal [27] for a ground-breaking application in personal protective equipment (PPE). The motivation lies in the growing interest in the use of these technologies [28] for the production of high-performance PPE (sports [29], military [30]) and other biomedical applications [28]. The specification for such devices is the high levels of impact absorbency and the lightness. For enhancing these properties, the current studies were mainly based on using bio-inspired shapes [31,32], lattice structures [29], and topology optimized [32] parts. In light of the literature summary reported above, 3D fractal geometries could represent a perfect innovative candidate for PPE applications. This work investigates the mechanical properties of 3D Greek cross fractal geometry produced in polyamide 12 (PA12) by selective laser sintering (SLS). Mechanical performances in the quasi-static compression tests are numerically simulated by a finite element (FE) model and validated experimentally.

2. Material and methods

2.1. Greek cross-based fractal design

A fractal geometry results from subsequent transformations of a simple geometric object (line, triangle, square, etc.) defined as “initiator” [2]. Based on deterministic or stochastic rules, these transformations usually follow recursive formulations in the field of real or complex numbers. The simplest fractal construction method is based on affine transformations such as scaling, translation, rotation, reflection, and a combination of them [1].

The fractal structure used in this study is inspired by the mathematical 3D Greek cross presented by Dickau R. [27]. The initiator consists of a cross of three struts linearly extruded along the axes of a cartesian tern (Fig. 1). Each strut has a circular cross-section of diameter D_s that is constant at each n^{th}-step. At step n=1, the initiator consists of three struts whose length is equal to L_1^{st}. These struts cross at the origin point of the cartesian tern by generating six branches of size equal to $L_1^{st}/2$. At n^{th}-step, each branch of length $L_n^{th}{}_{-1}/2$ is assumed to be one of the three struts along principal axes; therefore, two struts of length $L_n^{th}{}_{-1}/2$ are added along the remained axes; these construction rules make the number of branches equal to 6^n at step n^{th}.

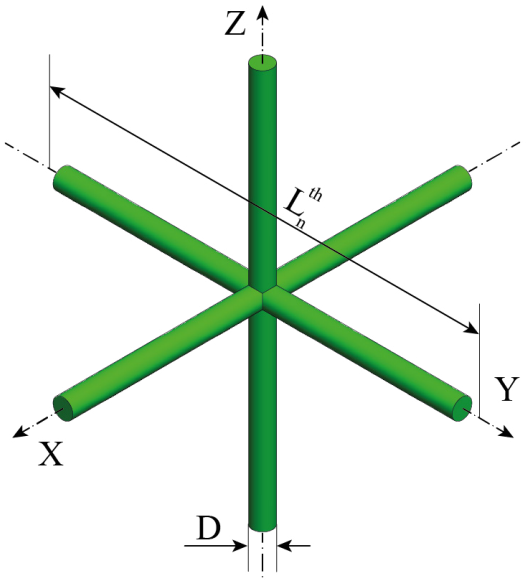

Fig.1. 3D Greek cross initiator geometric dimensions.

The transformation series of the structure stop within two iterations at the 3rd step. However, from a mathematical point of view, it can be demonstrated that the final generated structure tends to be an octahedron for the n^{th}-step tending to infinity. Fig. 2 shows the iteration steps used to generate the 3D cross-based fractal structure (3D-CFS).

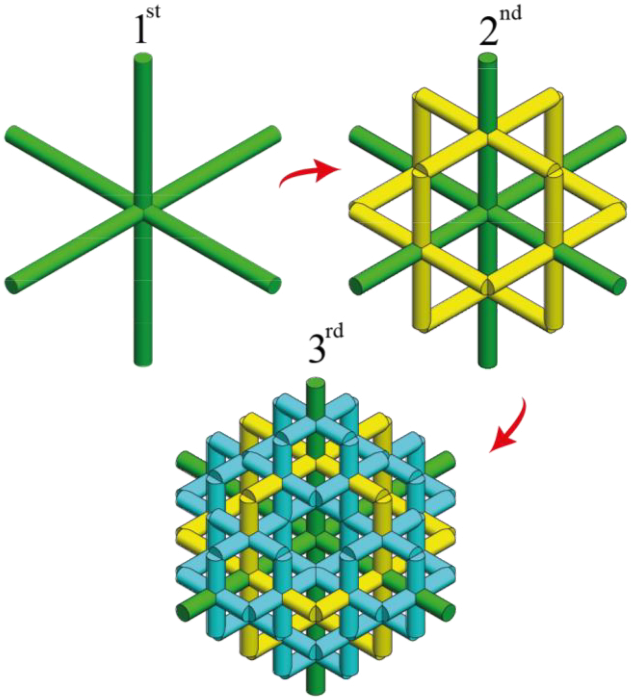

Fig. 2. 3D-CFS iterations: in green the first step, in yellow the added axes of the second step, and in light blue the added axes of the third step.

The design of the 3D-CFS is parametric, and its overall size depends on the two main parameters cited above, L_n^{th} and D_s. Therefore, its dimension can be tailored by considering the production system, the material, and the final application of the

structure. The design proposed for the experimental tests consisted of a 3D-CFS developed in a cubic envelope of 40 mm side and 2 mm long diameter struts. Over successive iterations, owing to the scale factor of strut length equal to 1/2, the deriving branches overlap at either end. This overlapping generates sharp edges around which stress concentration presence may occur when the structure is loaded. Also, for assembly purposes, these extremities require adjustments. Thus, chamfers were added, as Fig. 3a shows.

To evaluate the mechanical properties of the 3D-CFS, a cubic compressive test sample was developed by simulating a single repetitive cell of a multi-structure system. First, a single 3D-CFS was linearly replicated in the space (Fig. 3b-left); then, a region of interest corresponding to a cube of 40 mm side was extracted. Two square bases of 42 mm side and 2 mm thick have been added as continuous interfaces with the structure (Fig. 3c). These plates were used to apply the quasi-static compressive load.

2.2. Production and testing

The samples were manufactured in PA2200 (trade name of EOS GmbH of PA12) with the Formiga P110 Velocis (EOS GmbH) As suggested by the supplier, the PA2200 material was used as a mixture of 50% virgin and 50% recycled powder. The main properties of the material are reported in Table 1 [33]. Table 3 reports the process parameters used for the production.

Table 1. Datasheet PA2200 [33].

Tensile modulus *[MPa]*	1650
Tensile strength *[MPa]*	48
Elongation at break *[%]*	18
Melting temperature *[°C]*	176
Bulk density *[g/cm^3]*	0.45
Density of laser-sintered part *[g/cm^3]*	0.93

Table 2. Formiga P110 Velocis process parameters for PA2200 material.

Parameter	
Process chamber temperature *[°C]*	172
Removal chamber temperature *[°C]*	154
Laser power *[W]*	21
Scan speed *[mm/s]*	2500
Hatch distance *[mm]*	0.25
Layer thickness *[mm]*	0.100

The mechanical properties of the PA2200 material were experimentally evaluated by tensile tests. The universal testing machine AURA Easydur was used to perform the tests. The device is equipped with a 10 tonnes load cell, servo-electric actuator, and pneumatic wedge action grips. According to the EN ISO 527-2:2012 [34], the crosshead speed of the tensile test was set to 5 mm/min, corresponding to a 2 x 10^{-3} s^{-1} strain rate. The software of the machine records the testing data with a sampling rate of 500 Hz. The strain data were recorded through an extensometer with a gauge length of 49 mm.

Five replicas of the 3D-CFS sample were produced. The plates of each sample were oriented parallel to the build platform. After the production, quasi-static compression tests were performed using a universal testing machine, 3MZ Easydur, equipped with a load cell of 5 tonnes. The crosshead speed for the compression tests was set to 5 mm/min. The sampling rate was equal to 100 Hz. The strain (ε_e) was calculated considering the crosshead displacement (Δl) with a gauge length equivalent to the structure height (l_0). The nominal stress was calculated as the ratio of response force (F) measured by the load cell and the nominal area of the structure (minimum cross-section A_0) extrapolated by the CAD file. Eq. 1 and Eq. 2 report the formulas used to calculate the engineering strain and stress.

$$\varepsilon_e = \frac{\Delta l}{l_0} \tag{1}$$

$$\sigma_e = \frac{F}{A_0} \tag{2}$$

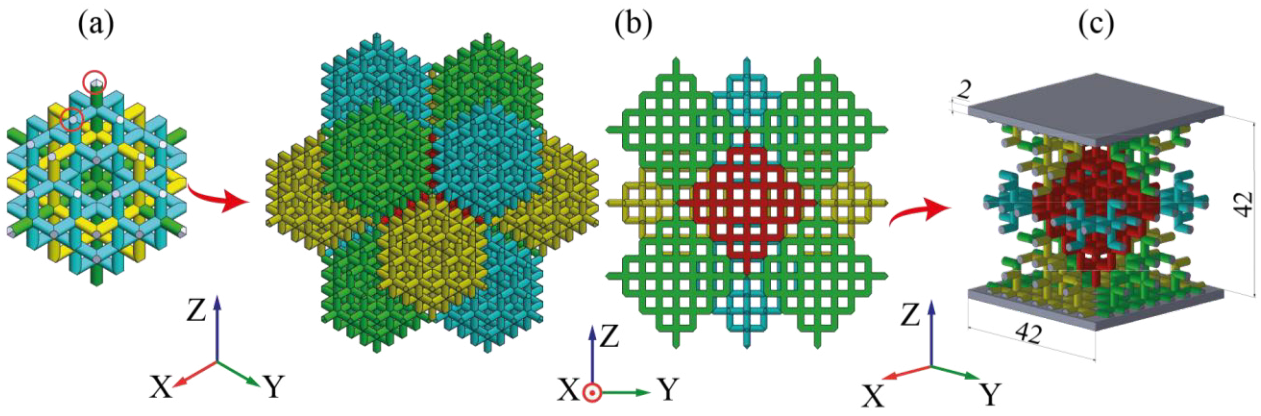

Fig. 3. (a) Chamfers adding (red circle); (b) space replication (left) and lateral-section (right); (c) cubic sample after cuts.

To evaluate the energy absorption performance of a structure, it is a common practice to refer to the energy absorption formula W, which represents the area under the stress-strain curve [35], and it is computed as Eq. 3 shows:

$$W = \int_0^{\varepsilon} \sigma(\varepsilon) d\varepsilon \quad (3)$$

In addition, to taking into account the material properties of the absorber, it is required to evaluate the specific energy absorption (SEA), which is defined in Eq. (4) as the ratio between the work W performed by the structure under compression and the material density [36].

$$SEA = \frac{W}{\rho} \quad (4)$$

2.3. Numerical simulations

The numerical tests of the 3D-CFS have been modelled and solved using the finite element method. The CAD file model was meshed using Hypermesh, and the FE model was implemented in HyperWorks 2021 by Altair®. All the numerical simulations were solved using the RADIOSS® solver.

2.3.1. Material modelling

The polyamide was modelled as an elastoplastic isotropic material. Additionally, an implicit non-linear analysis was performed to better simulate a mechanical test under quasi-static load conditions. The material model selected for the PA2200 is the elastic-plastic piecewise linear material (/MAT/LAW36) [37]. The plastic curve obtained from tensile tests was implemented as input in the material model. Because of the large plastic deformation before the failure point of the polyamide, the engineering stress-strain curve was converted into a true stress-strain curve by using Eq. 5 and Eq. 6. Because of the non-linear behavior of the material, the beginning of the plastic field (yield point) was assumed as the true stress value corresponding to 0.2% true strain. Then, the plastic strain was computed using Eq. 7 within the range of the yield point and the maximum stress value. The obtained true stress versus yield-strain curve was implemented as material law in the FE software.

$$\varepsilon_{tr} = ln(1 + \varepsilon_e) \quad (5)$$

$$\sigma_{tr} = \sigma_e \cdot e^{\varepsilon_{tr}} \quad (6)$$

$$\varepsilon_{pl} = \varepsilon_{tr} - \frac{\sigma_{tr}}{E} \quad (7)$$

The mechanical properties of the material for the numerical model calibration were obtained by using dog-bone specimens produced in two different orientations with respect the build volume. Five replicas for each orientation were manufactured and tested by a uniaxial tension test.

The tensile modulus was set equal to the statistic average value obtained by the experimental tensile test (E=1643 MPa). According to the material datasheet, density and Poisson ratio were set equal to 0.93 g/cm^3 and 0.39, respectively. To validate the developed material model, the tensile test was modelled and simulated in RADIOSS. To simulate the material's failure behavior, it was activated the failure model (FAIL/BIQUAD) that uses a non-linear strain-based failure criterion described by a bi-quadratic function. This model requires as input the plastic failure strain value obtained experimentally by different load conditions. The calibration of the failure model was performed by varying the failure coefficient and comparing the experimental results with the numerical curve.

2.3.2. Compression test modelling

The simulation of the compression test was carried out by setting a non-linear quasi-static implicit analysis in the large displacements field. A self-contact interaction was imposed among the struts with a friction coefficient equal to 0.3. The 3D-CFS structure was discretized by 4-nodes tetrahedral elements (TETRA4) with an adaptive element size ranging between 0.2 mm and 6 mm. The mesh size depended on strut diameter dimension and SLS process resolution. The compression was simulated by imposing a velocity of 0.083 mm/s to a node connected rigidly to the top surface of the top plate. Moreover, the top plate was constrained to the only movement along with the load, while the bottom plate was fully constrained.

3. Results and discussion

3.1. Compression test results

Fig. 4 (blue curve) shows the experimental results obtained by the compression test on the fractal structure. The simulations of the 3D-CFS structure compression test were performed both neglecting (Fig. 4 – orange curve) or considering the strut damage or break (Fig. 4 – grey curve). The failure mode was implemented because of the fracture of the structure in a few localized nodes observed experimentally at around 5% of strain. These fractures induce a sudden decrease in the strength of the structure and, consequently, a fragmentation of the plateau region. Therefore, the failure mode was implemented in the numerical model.

Fig. 4 highlights the differences between the two developed numerical models in comparison with the experimental results. Both models overestimate the mechanical behavior of the structure. However, the model with the activation of the failure mode can well predict the bending behavior of the struts and the related fractures. In contrast, the model with no failure mode reports a constant plateau with a higher densification starting point than the second model.

Overall, the deviation between the experimental and numerical results is constant along with the simulation. This means that there is a systematic effect that has been neglected in the modelling. This effect can be attributed to the manufacturing process, such as internal porosity or roughness, which hardly can be accurately considered in the modelling.

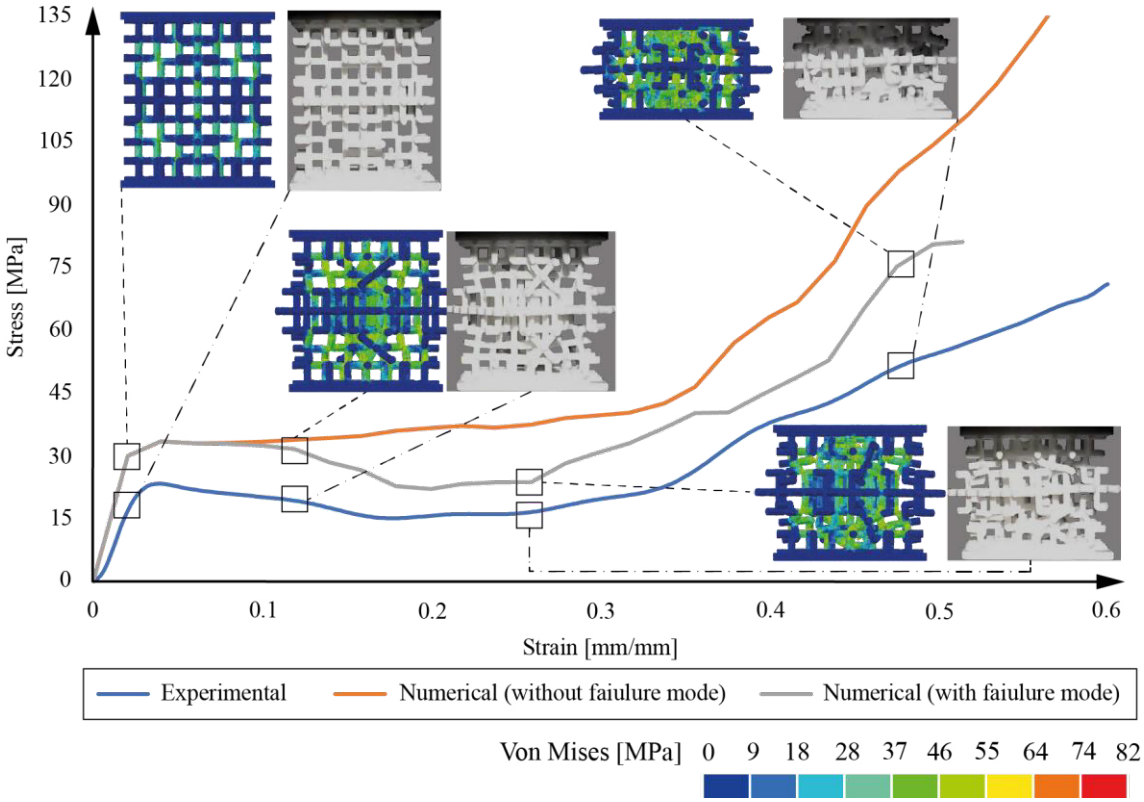

Fig. 4. Comparison between the experimental and numerical results of the 3D-CFS structure.

3.2. Energy absorption performance

The energy absorption performance of 3D-CFS was compared to an expanded polystyrene foam used typically as absorber material for helmets protection, EPS-60. The stress-strain curve of EPS-60 available in the literature [38] is reported in Fig. 5a.

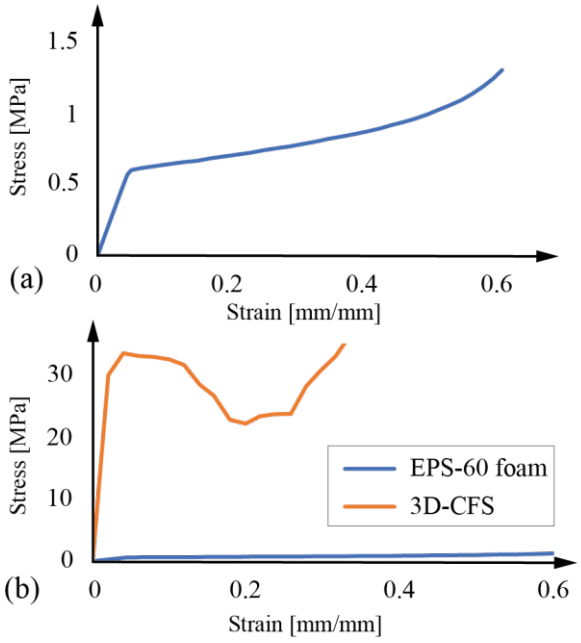

Fig. 5. (a) Stress-strain curve of EPS-60 foam [38]. (b) Comparison between EPS-60 foam and 3D-CFS structure tested under quasi-static compression load.

The total energy up to the start of densification area (assumed 30% strain) is reported in Table 3. Fig. 5b shows that the areas under the stress-strain curves obtained from the different materials are significantly different. This difference is strictly related to the material densities, which are not comparable (see Table 3). Because of that, the evaluation of the total energy may lead to an incorrect assessment. For this reason, the specific energy absorption (SEA) is a better descriptor for material performance comparison.

The SEA values of EPS-60 and 3D-CFS obtained by computing Eq. 4 are reported in Table 6. Remarkably, the 3D-CFS structure analyzed in this work can absorb up to 65% more energy with respect to the typical EPS foam.

Table 3. Energy absorption performance comparison between EPS-60 foam, 3D-CFS.

		EPS-60 foam	3D-CFS
$\boldsymbol{\rho}$	$[kg/m^3]$	60	930
$\boldsymbol{W_{\varepsilon=30\%}}$	$[J/mm^3]$	0.21	9.4
$\boldsymbol{SEA}$	$[kJ/kg]$	3.5	10.1

4. Conclusion

In this study, a 3D fractal structure was designed for impact absorption applications and produced by the SLS additive manufacturing technique in PA2200 material. A finite element model was developed to numerically simulate the designed structure's mechanical behavior under quasi-static compression loads. The compression test results show that the induced manufacturing defects can reduce the mechanical performance

when compared to the numerical simulation The FE model offers excellent energy absorption performance, showing up to 65% higher SEA compared to a typical foam used for personal protective equipment. These results suggest the enormous capabilities in designing high mechanical performance components by exploring fractal geometries and combining them with additive manufacturing processes.

References

[1] Peitgen, H.-O., H. Jürgens, D. Saupe, Chaos and fractals: new frontiers of science, Springer Science & Business Media, 2006.

[2] Mandelbrot, B.B., Les objets fractals: forme, hasard et dimension, (1975).

[3] Barnsley, M.F., Fractals everywhere, Academic press, 2014.

[4] OLÓRIZ, F., P. PALMQVIST, J.A. PÉREZ-CLAROS, Shell features, main colonized environments, and fractal analysis of sutures in Late Jurassic ammonites, Lethaia. 30 (1997) 191–204.

[5] Losa, G.A., Fractals in biology and medicine, Rev. Cell Biol. Mol. Med. (2006).

[6] Mandelbrot, B., How long is the coast of Britain? Statistical self-similarity and fractional dimension, Science (80-.). 156 (1967) 636–638.

[7] Encarnação, J.L., H.-O. Peitgen, G. Sakas, G. Englert, Fractal geometry and computer graphics, Springer Science & Business Media, 2012.

[8] Ehret, A.E., M. Hollenstein, E. Mazza, M. Itskov, Dynamical characterization of mixed fractal structures, 6 (2011).

[9] Alia, M., K. Suwais, Improved steganography scheme based on fractal set, Int. Arab J. Inf. Technol. 17 (2020) 128–136. https://doi.org/10.34028/iajit/17/1/15.

[10] Sotillo, J.U., A.D. Lantada, Incorporation of Fractal Textures to 3D CAD: Towards an Enhanced Control of Surface Topography, Comput. Aided. Des. Appl. 12 (2015) 135–146. https://doi.org/10.1080/16864360.2014.962426.

[11] Gong, Y., J. Shen, W. Liu, L. Chen, Fractal characteristics of mechanical interface contact parameters, MATEC Web Conf. 175 (2018) 1–5. https://doi.org/10.1051/matecconf/201817503009.

[12] Li, Y., C. Ortiz, M.C. Boyce, Bioinspired, mechanical, deterministic fractal model for hierarchical suture joints, Phys. Rev. E - Stat. Nonlinear, Soft Matter Phys. 85 (2012) 1–14. https://doi.org/10.1103/PhysRevE.85.031901.

[13] Khoshhesab, M.M., Design, Mechanical Modeling and 3D Printing of Koch Fractal Contact and Interlocking, University of New Hampshire, 2017.

[14] Wang, G., Y. Gu, L. Zhao, J. Xuan, G. Zeng, Z. Tang, Y. Sun, Experimental and numerical investigation of fractal-tree-like heat exchanger manufactured by 3D printing, Chem. Eng. Sci. 195 (2019) 250–261. https://doi.org/10.1016/j.ces.2018.07.021.

[15] Paniagua-Guerra, L.E., S. Sehgal, C.U. Gonzalez-Valle, B. Ramos-Alvarado, Fractal channel manifolds for microjet liquid-cooled heat sinks, Int. J. Heat Mass Transf. 138 (2019) 257–266. https://doi.org/10.1016/j.ijheatmasstransfer.2019.04.039.

[16] Ha, N.S., T.M. Pham, W. Chen, H. Hao, G. Lu, Crashworthiness analysis of bio-inspired fractal tree-like multi-cell circular tubes under axial crushing, Thin-Walled Struct. 169 (2021) 108315. https://doi.org/10.1016/j.tws.2021.108315.

[17] Wu, J., Y. Zhang, F. Zhang, Y. Hou, X. Yan, A bionic tree-liked fractal structure as energy absorber under axial loading, Eng. Struct. 245 (2021) 112914. https://doi.org/10.1016/j.engstruct.2021.112914.

[18] Zhang, Y., M. Lu, C.H. Wang, G. Sun, G. Li, Out-of-plane crashworthiness of bio-inspired self-similar regular hierarchical honeycombs, Compos. Struct. 144 (2016) 1–13. https://doi.org/10.1016/j.compstruct.2016.02.014.

[19] Zhang, Y., J. Wang, C. Wang, Y. Zeng, T. Chen, Crashworthiness of bionic fractal hierarchical structures, Mater. Des. 158 (2018) 147–159. https://doi.org/10.1016/j.matdes.2018.08.028.

[20] Li, Z., L. Shen, K. Wei, Z. Wang, Compressive behaviors of fractal-like honeycombs with different array configurations under low velocity impact loading, Thin-Walled Struct. 163 (2021). https://doi.org/10.1016/j.tws.2021.107759.

[21] Liu, H., E.T. Zhang, B.F. Ng, In-plane dynamic crushing of a novel honeycomb with functionally graded fractal self-similarity, Compos. Struct. 270 (2021) 114106. https://doi.org/10.1016/j.compstruct.2021.114106.

[22] Wang, J., Y. Zhang, N. He, C.H. Wang, Crashworthiness behavior of Koch fractal structures, Mater. Des. 144 (2018) 229–244. https://doi.org/10.1016/j.matdes.2018.02.035.

[23] Dadrasi, A., M. Beynaghi, S. Fooladpanjeh, Crashworthiness of Thin-Walled Square Steel Columns Reinforced Based on Fractal Geometries, Trans. Indian Inst. Met. 72 (2019) 215–225. https://doi.org/10.1007/s12666-018-1475-9.

[24] Zhang, Y., N. He, X. Song, T. Chen, H. Chen, On impacting mechanical behaviors of side fractal structures, Thin-Walled Struct. 146 (2020) 106490. https://doi.org/10.1016/j.tws.2019.106490.

[25] He, Q., Y. Wang, H. Gu, J. Feng, H. Zhou, The dynamic behavior of fractal-like tubes with Sierpinski hierarchy under axial loading, Eng. Comput. (2021). https://doi.org/10.1007/s00366-020-01275-6.

[26] Calignano, F., D. Manfredi, E.P. Ambrosio, S. Biamino, M. Lombardi, E. Atzeni, A. Salmi, P. Minetola, L. Iuliano, P. Fino, Overview on additive manufacturing technologies, Proc. IEEE. 105 (2017) 593–612. https://doi.org/10.1109/JPROC.2016.2625098.

[27] Dickau, R., Greek Cross Fractal, (2008). https://www.robertdickau.com/greekcross.html (accessed February 10, 2022).

[28] Jafferson, J.M., S. Pattanashetti, Use of 3D printing in production of personal protective equipment (PPE) - A review, Mater. Today Proc. 46 (2021) 1247–1260. https://doi.org/10.1016/j.matpr.2021.02.072.

[29] Khosroshahi, S.F., S.A. Tsampas, U. Galvanetto, Feasibility study on the use of a hierarchical lattice architecture for helmet liners, Mater. Today Commun. 14 (2018) 312–323. https://doi.org/10.1016/j.mtcomm.2018.02.002.

[30] Rice University, Rice tapped to develop 3D-printed 'smart helmets' for the military, (n.d.). https://news.rice.edu/news/2021/rice-tapped-develop-3d-printed-smart-helmets-military.

[31] Mehta, P.S., J. Solis Ocampo, A. Tovar, P. Chaudhari, Bio-Inspired Design of Lightweight and Protective Structures, SAE Tech. Pap. (2016). https://doi.org/10.4271/2016-01-0396.

[32] Najmon, J.C., J. Dehart, Z. Wood, A. Tovar, Cellular Helmet Liner Design through Bio-inspired Structures and Topology Optimization of Compliant Mechanism Lattices, SAE Int. J. Transp. Saf. 6 (2018) 217–235. https://doi.org/10.4271/2018-01-1057.

[33] EOS GmbH - Electro Optical Systems, Material data sheet PA 2200, 2017. https://www.eos.info/en/additive-manufacturing/3d-printing-plastic/sls-polymer-materials/polyamide-pa-12-alumide.

[34] ISO, U.E., British Standards Institution, BS EN ISO 527-2:2012. Plastics-Determination of tensile properties-Part 2: Test conditions for moulding and extrusion plastics, 2012.

[35] Belingardi, G., R. Montanini, M. Avalle, Characterization of polymeric structural foams under compressive impact loading by means of energy-absorption diagram, Int. J. Impact Eng. 25 (2001) 455–472.

[36] Tancogne-Dejean, T., A.B. Spierings, D. Mohr, Additively-manufactured metallic micro-lattice materials for high specific energy absorption under static and dynamic loading, Acta Mater. 116 (2016) 14–28. https://doi.org/10.1016/j.actamat.2016.05.054.

[37] Hodge, P.G., H.G. Hopkins, E.H. Lee, The theory of piecewise linear isotropic plasticity, in: Deform. Flow Solids/Verformung Und Fliessen Des Festkörpers, Springer, 1956: pp. 147–170. https://doi.org/10.1007/978-3-642-48236-6_14.

[38] de Sousa, R.A., R. Coelho, F. Teixeira-Dias, D. Gonçalves, Assessing the effectiveness of a natural cellular material used as safety padding material in motorcycle helmets, Simulation. 88 (2012) 580–591. https://doi.org/10.1177/0037549711414735.